Unveiling nonmonotonic chemical trends in the solubility of H in complex Fe-Cr-Mn carbides by means of ab initio based approaches

Sreekala, Lekshmi; Dey, Poulumi; Hickel, Tilmann; Neugebauer, Jörg

DOI
10.1103/PhysRevMaterials.6.014403

Publication date
2022

Document Version
Final published version

Published in
Physical Review Materials

Unveiling nonmonotonic chemical trends in the solubility of H in complex Fe-Cr-Mn carbides by means of *ab initio* based approaches

Lekshmi Sreekala [1,*] Poulumi Dey [2] Tilmann Hickel [1,3] and Jörg Neugebauer [1]

[1]*Department of Computational Material Design, Max-Planck-Institut für Eisenforschung, Max-Planck-Strasse 1, 40237 Düsseldorf, Germany*

[2]*Department of Materials Science and Engineering, Delft University of Technology, 2628 CD Delft, The Netherlands*

[3]*BAM Federal Institute for Materials Research and Testing, Richard-Willstätter-Str. 11, 12489 Berlin, Germany*

(Received 7 September 2021; revised 30 November 2021; accepted 22 December 2021; published 18 January 2022)

The microstructure of advanced high-strength steels often shows a sensitive dependence on alloying. For example, adding Cr to improve the corrosion resistance of medium-Mn steels also enhances the precipitation of carbides. The current study focuses on the behavior of H in such complex multicomponent carbides by employing different methodological strategies. We systematically analyze the impact of Cr, Mn, and Fe using density functional theory (DFT) for two prototype precipitate phases, M_3C and $M_{23}C_6$, where M represents the metal sublattice. Our results show that the addition of these alloying elements yields strong nonmonotonic chemical trends for the H solubility. We identify magnetovolume effects as the origin for this behavior, which depend on the considered system, the sites occupied by H, and short- vs long-range interactions between H and the alloying elements. We further show that the H solubility is directly correlated with the occupation of its nearest-neighbor shells by Cr and Mn. Based on these insights, DFT data from H containing binary-metal carbides are used to design a ridge regression based model that predicts the solubility of H in the ternary-metal carbides (Fe-Cr-Mn-C).

DOI: 10.1103/PhysRevMaterials.6.014403

I. INTRODUCTION

In the past years, the excellent mechanical properties of high-manganese steels (HMnS) that show transformation induced plasticity (TRIP) or twinning-induced plasticity (TWIP) have gained increased scientific and commercial interest, for instance, in automotive industries [1–4]. While a lot of effort has been made to optimize the strength and ductility of HMnS, their hydrogen induced delayed fracture is still an issue of critical importance [5,6]. The mechanisms giving rise to the accumulation of hydrogen atoms, which are usually introduced during production and application, in critical regions like grain boundaries and dislocations are not yet fully understood. Also, crack formation and propagation that ultimately lead to the failure of the material are subjects of investigations [7–9]. Nevertheless, it is well known that the susceptibility to hydrogen embrittlement (HE) is correlated with the microstructural characteristics of the material [10,11].

The main challenge in designing advanced HMnS is to improve multiple properties by alloying, for example, reducing the susceptibility to HE, without being detrimental to strength or ductility. One possible alloying strategy is to introduce microstructural features like precipitates. Such precipitates play a major role in the strengthening mechanism of steels along with their capacity to trap infused hydrogen [12–14]. The incorporation of alloying elements like Cr and Mn that have a strong carbide forming tendency [15–17] controls the stability of Fe carbides like Fe_3C or $Fe_{23}C_6$ without compromising other mechanical properties [18–20]. In addition, Cr introduced into steels improves the corrosion resistance and hardenability of the material, which is relevant for applications [21,22]. However, a systematic analysis on the H interactions in such Cr containing carbides in industrial high-Mn steels is lacking.

Various iron carbides with different crystal structures and physical properties exist. Among them, the cementite phase (Fe_3C) is found more commonly in steels than other carbides [23]. It crystallizes in an orthorhombic unit cell with 12 Fe atoms and 4 carbon atoms. Another relatively stable iron carbide which has a formation enthalpy comparable to that of Fe_3C is $Fe_{23}C_6$ [24]. It is a complex iron carbide phase with a face-centered cubic structure. The conventional unit cell consists of 92 Fe atoms and 24 carbon atoms [25,26]. Among $(Fe, Cr, Mn)_{23}C_6$, only $Cr_{23}C_6$ is a stable carbide, which has been studied by experimental and theoretical approaches regarding its crystal and thermodynamic properties [27–29].

One of the important open questions is the role of Cr and Mn on HE in the context of carbide formation. As an essential part of the microstructure, the carbides will strongly affect the mobility, trapping, and release as well as decohesion effects of hydrogen. These effects can occur both in the carbide bulk as well as at the interface to the matrix [14,30]. The focus

*Corresponding author: l.sreekala@mpie.de

of the present investigation is to understand on an atomistic scale the impact of the actual composition of the carbide on the solubility of H. This is a question of central interest, because the solubility range of alloying elements, i.e., the range of possible compositions, is much larger in the carbides than in the matrix material of a multicomponent steel. At the same time, this is a challenge for advanced modeling approaches. Multicomponent carbides containing Fe, Cr, and Mn impose next to the chemical also magnetic and structural complexities. Together, they give rise to surprisingly complex nonmonotonic H solubility trends when changing alloy composition, as revealed in this work.

Ab initio simulation techniques based on quantum mechanical approaches are perfectly suited to understanding the significance of these degrees of freedom on H solubilities [31–33]. However, DFT based calculations are computationally expensive and have been performed only for binary alloys so far. The present work addresses these challenges by combining the in-depth analysis from *ab initio* methods with the statistical sampling by basic machine learning approaches.

As prototype precipitates in steels, we study carbides like M_3C and $M_{23}C_6$, where M is a mixture of Fe, Cr, and Mn, together with their susceptibility towards HE. Within these carbides, H atoms can either be located at interstitial sites or at C vacancies [see Fig. 2(a)]. Here, a C vacancy-H refers to the occupation of H in a C vacant site [34,35], while the interstitial sites are those sites that are not occupied by C atoms in defect-free regions of the carbides. Though these phases have been observed in different Fe-based alloys, steels, and minerals [36], detailed theoretical knowledge about their chemical composition and their affinity towards H, as well as the electronic and magnetic properties, is still rare.

The eventual goal of our investigations is to understand the behavior of H in a microstructure like pearlite that contains the Fe-Cr-Mn-C carbides, the ferritic or austentic matrix phase, and the corresponding interfaces with the presence and absence of alloying elements. However, this modeling poses a big challenge to first-principles calculations, because of the large lattice mismatch at the interfaces, especially between ferrite and $M_{23}C_6$. Therefore, we restrict our study to identifying the chemical trends for H solubilities in bulk M_3C and $M_{23}C_6$ where M is a mixture of Cr-Fe, Mn-Fe, and Cr-Mn separately and to establish correlations between these binary-metal carbides (Fe-M-C). By generating a machine learning algorithm based on the H solubility data from binary-metal carbide systems, we predict H solubilities that correspond to ternary-metal carbides (Fe-Cr-Mn-C). As a step towards defects, we further extend our study to vacancies in the bulk phases. Based on the achieved insights about the underlying mechanisms, we believe that these methods and insights can also be transferred to the behavior at the interface in upcoming studies.

II. METHODOLOGY

The chemical, structural, and magnetic complexity of Fe-Cr-Mn-C carbides outlined above requires a dedicated strategy for the H interaction studies, which is schematically outlined in Fig. 1. One of the main features is that the detailed DFT investigations focus on binary-metal carbides,

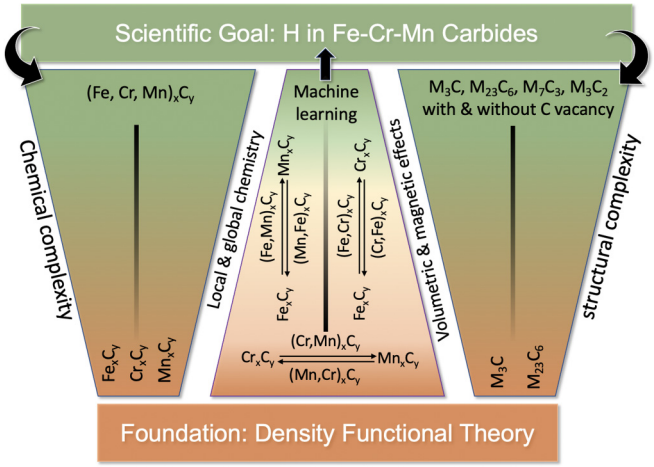

FIG. 1. General scheme for implementing the H interactions in multicomponent carbides. DFT calculations of H solubilities are performed for various compositions in interstitial and C vacancy sites. The studies are first carried out over a range of Cr and Mn concentrations separately in two different types of carbides. The obtained data are further used for implementing a machine learning approach to derive the solubility profile of H in Fe-Cr-Mn carbides.

e.g., $(Fe,Mn)_xC_y$, as a preliminary step. This will allow us to understand the physical phenomena controlling the H solubility trends in carbides containing Cr and Mn. To this end, we decompose the chemical complexity into a short- and long-range chemical contribution around H along with the magnetic and volumetric effects of the system. Computing the H solution energy of all possible interstitials, we select the sites corresponding to minimum energies for our study. Finally, a machine learning approach is employed to predict the solubility of H in Fe-Cr-Mn-C systems based on an informed training set for the H behavior in binary-metal carbide systems. To capture the structural complexity, two extensions are further considered: the transfer from perfect carbides to those containing C vacancies and the transfer from carbides of the structure M_3C to the structure $M_{23}C_6$.

The influence of the substitutional elements Cr or Mn on the H solubility is evaluated by performing systematic trend studies. There exist a variety of configurations for substituting these alloying elements in the metal sublattice of the carbides. We distinguish first and higher order nearest-neighbor (NN) shells, because their impact is found to be different. A two-step approach is used to reduce the chemical complexity: we first analyze the dependence on the substitution in the first NN shell, keeping the rest of the supercell in the pure Fe state [see Fig. 2(b)]. In a second step, the effects of alloying in the shells away from the H atom are considered, keeping the first NN shell completely substituted by Cr or Mn and filling the shells with the shortest distance first [see Fig. 2(c)]. In this way, the Fe-rich and the substitution rich conditions are handled in one sequence of calculation. This methodological approach is chosen under the consideration that the arrangement of metal and carbon atoms occurs during the thermochemical processing of the steels and is not subject to site changes at the time hydrogen enters. Further, this chosen approach provides chemical trends close to the behavior of H in reality: in case

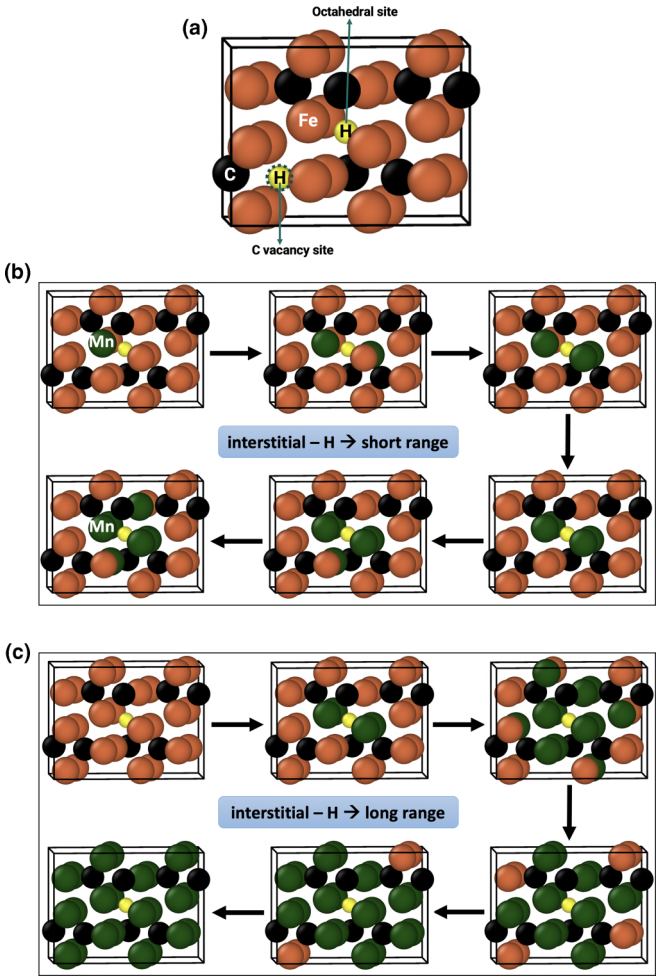

FIG. 2. (a) Crystal structure of Fe_3C including the preferred interstitial site and the alternative C vacancy site for H. The shell structure of interstitial-H contains 6, 2, and 6 metal atoms in first nearest, second, and third neighbor shell, respectively. (b) Study of the interaction of H (yellow spheres) with neighboring Fe (brown spheres) and substitutional elements (green spheres). Starting from Fe_3C with H at the interstitial site, configurations with increasingly many Fe atoms in the nearest neighbor shell (short range) of H, ordered according to their distance from H, are replaced by Mn for the discussion in Sec. III A and Sec. III C. (c) Configurations with increasingly many Mn atoms in the second and higher shells (long range) up to a full occupancy of the metal sublattice are considered. The same methodology is used to study the solubility of H in C vacancy sites of Fe_3C and $Fe_{23}C_6$.

of low concentrations of the alloying elements (Cr and Mn), H energetically prefers NN sites of the solute. Long-range interactions are only relevant if the concentration of Cr and Mn is high. For a statistically relevant data set required for the training of the machine learning model, however, also configurations with a few solutes in long-range distance from H are taken into account, i.e., the impact of Fe, Mn, and Cr is treated consistently (see Fig. 1), independent of the energetics.

The solution enthalpy of a H atom in any of these configurations is calculated using

$$\Delta H_H = E_{\rm tot}[{\rm M_xC_yH}] - E_{\rm tot}[{\rm M_xC_y}] - \mu_{\rm H} \qquad (1)$$

where M can be Fe, Cr, Mn, or combinations of them and the chemical potential $\mu_{\rm H}$ of H is determined by assuming a chemical equilibrium of H in the carbides and the matrix. For the solution enthalpy of a H atom at the C site, one can consider two scenarios: a substitution of C by H has the formation energy

$$\begin{aligned}\Delta H_H^{Cvac} &= E_{\rm tot}[{\rm M_xC_{y-1}H}] - E_{\rm tot}[{\rm M_xC_y}] \\ &\quad + \mu_{\rm C} - \mu_{\rm H} \qquad (2)\\ &= (E_{\rm tot}[{\rm M_xC_{y-1}H}] - E_{\rm tot}[{\rm M_xC_{y-1}}] - \mu_{\rm H}) \\ &\quad + (E_{\rm tot}[{\rm M_xC_{y-1}}] - E_{\rm tot}[{\rm M_xC_y}] + \mu_{\rm C}). \qquad (3)\end{aligned}$$

Here, the second term of (3) is the C vacancy formation energy and the chemical potential reference of C, $\mu_{\rm C}$, is the energy of a C atom in the octahedral site of bcc Fe. However, the absolute formation energies of C vacancies in Cr and Mn containing carbides are typically much larger (all the values are above 0.9 eV [37] for M_3C and $M_{23}C_6$ carbides) than the H solution enthalpies, which makes this process unlikely to happen. If in a second scenario, vacancies are assumed to be present due to independent processes (such a presence has been reported previously [38]), then the relevant term for the H solution enthalpy considered in this work is the first term of Eq. (3), which is identical with the H solution enthalpy in Eq. (1). Therefore, in contrast to the situation in other carbides [14], the substitution of C by H is less likely than the occupation of previously formed C vacancies by H atoms, i.e., we consider a model where the formation of the C vacancies is not part of the hydrogen solution enthalpy. A negative/positive solution enthalpy indicates higher/lower solubility. For the systematic study of solution enthalpies, interstitial H in pure bcc Fe at zero pressure and temperature is used as a reference, i.e., ignoring the impact of alloying elements in the matrix.

The concentration of H corresponding to its solution enthalpy is evaluated using a Boltzmann relation as follows:

$$c = c_0 \exp\left(\frac{-\Delta H_H}{k_B T}\right), \qquad (4)$$

where c_0 is the concentration of available interstitial sites. k_B denotes the Boltzmann constant and T is the temperature. To evaluate H concentrations at realistic conditions, the absolute value of the chemical potential can later be adjusted. A specific example is discussed in Sec. III E 2. While the absolute values of H solution enthalpies presented in Sec. III depend on $\mu_{\rm H}$, the trends discussed in this paper are independent of this choice.

To systematically investigate the relevant carbides precipitated in a high Mn steel sample (Fe-Mn-Al-Cr-C) with a Mn content of approximately 16 wt. % and a few percent of Cr, experimental studies are performed. Using energy dispersive x-ray spectroscopy (EDS) analysis of samples that were annealed at 650 °C for 100 h [Fig. 3(a)], it is revealed that the carbides are enriched in Cr and Mn along with relatively negligible amounts of Al and Fe. The EDS analysis of samples that were annealed at 500 °C [Fig. 3(b)] for 50 h provided information about a pearlitic area with proper distinction between the ferrite and carbide of higher C content. An extremely fine structure in the pearlite area later decomposes into the $M_{23}C_6$ carbide at 650 °C, where M stands for a mixture of Fe, Cr,

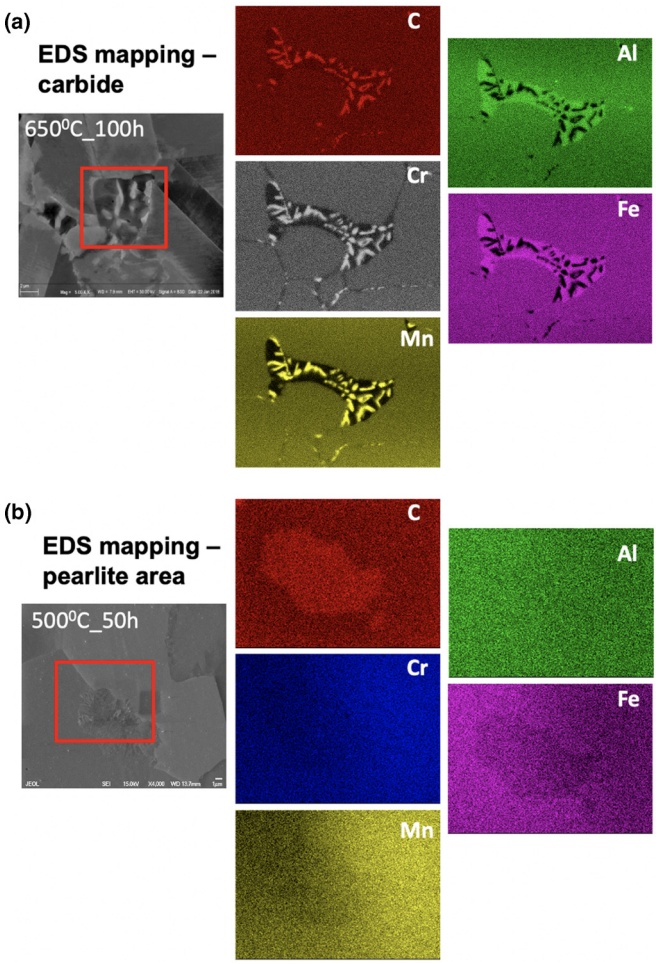

FIG. 3. EDS mapping of high-Mn steel sample at two different annealing temperatures are given. (a) EDS analysis of sample annealed at 650 °C shows the region of carbide and associated quantitative study of C, Cr, Mn, Al, and Fe. (b) EDS analysis of sample annealed at 500 °C shows the pearlite area in the sample providing the clear distinction between ferrite and carbide.

and Mn. The electron backscatter diffraction (EBSD) single pattern analysis on the sample concluded that the observed carbides are $M_{23}C_6$.

Computational details

We perform spin polarized DFT [39,40] calculations with the generalized gradient approximation (GGA) [41] functional form for electron exchange and correlation as introduced by Perdew, Burke, and Ernzerhof (PBE) [42]. To this end, the Vienna Ab Initio Simulation Package (VASP, version 5.4.1) [43–46] has been employed. The DFT calculations are performed in the framework of Blöchls projector augmented wave (PAW) method as implemented by Kresse and Joubert [47] with a kinetic energy cutoff of 520 eV for Fe_3C and $Fe_{23}C_6$ containing Cr and Mn, which we find is sufficient to converge the total energies within an accuracy of 1 meV/atom. The Brillouin zone integration is performed with the Monkhorst and Pack scheme [48] using k-point grids of $6 \times 12 \times 12$ and $6 \times 6 \times 6$ for a supercell of $2 \times 1 \times 1$ $(Fe,Cr/Mn)_3C$ and $1 \times 1 \times 1$ $(Fe,Cr/Mn)_{23}C_6$, respectively. The deviation of the H solution enthalpy values in comparison to the same in a $2 \times 2 \times 2$ supercell are below 10%. Partial band occupancies are considered using the smearing scheme of Methfessel and Paxton [49] with a σ value set to 0.2 eV. All the calculations were done at constant pressure by fully relaxing the supercells unless otherwise indicated. The lattice constants of the studied carbides and their comparison with existing experimental and other DFT works are given in Table I.

TABLE I. Lattice constants of Fe_3C and $Fe_{23}C_6$ compared with existing literature.

Fe_3C: Lattice constants (Å)			
	Present	Other DFT	Experiment
a	5.035	5.037[a], 5.035[b]	5.040[c]
b	6.715	6.720[a], 6.716[b]	6.730[c]
c	4.481	4.482[a], 4.480[b]	4.480[c]
$Fe_{23}C_6$: Lattice constants (Å)			
	Present	Other DFT	Experiment
a = b = c	10.466	10.467[a], 10.450[d]	10.639[e]

[a]Reference [24].
[b]Reference [50].
[c]Reference [51].
[d]Reference [52].
[e]Reference [53].

A ridge regression based machine learning algorithm is used to predict the solubility of H in ternary-metal carbides (Fe-Cr-Mn-C) with the DFT data of binary-metal carbides (Fe-Cr-C and Fe-Mn-C and Cr-Mn-C) used as the training set. Ridge regression is treated with L_2 regularization [54].

III. RESULTS

The behavior of H in Mn and Cr containing Fe_3C and $Fe_{23}C_6$ are studied at the interstitial sites, which are preferred by H [55], and additionally compared with C vacancy sites. This section is dedicated to understanding the influence of Mn addition to the H solubility in carbides for both short- and long-range interactions. Later, the role of Cr in determining H solubilities in carbides is investigated. Lastly, the transformation of the results from the *ab initio* approach into a machine learning model is discussed to predict the solubility of H in ternary-metal carbides.

A. Study on the short-range influence of Mn on the H solubility in Fe_3C

The short-range impact of Mn on the solution enthalpy of interstitial-H in $(Fe,Mn)_3C$ is visualized in Fig. 4(a) as a prototypical case. As a function of filling of the first NN shell of the H atom, a "V" shape dependence is observed up to four NN Mn atoms. More specifically, the solubility of H increases with the increase of the number of Mn atoms for the first two NN Mn atoms, decreases for the next two Mn atoms, and then remains nearly unchanged for the remaining two Mn atoms in the first NN shell. This strongly nonlinear and nonmonotonic behavior is in remarkable contrast to the linear Mn trend observed for the H solution enthalpy in fcc Fe-Mn solid solutions [32,56].

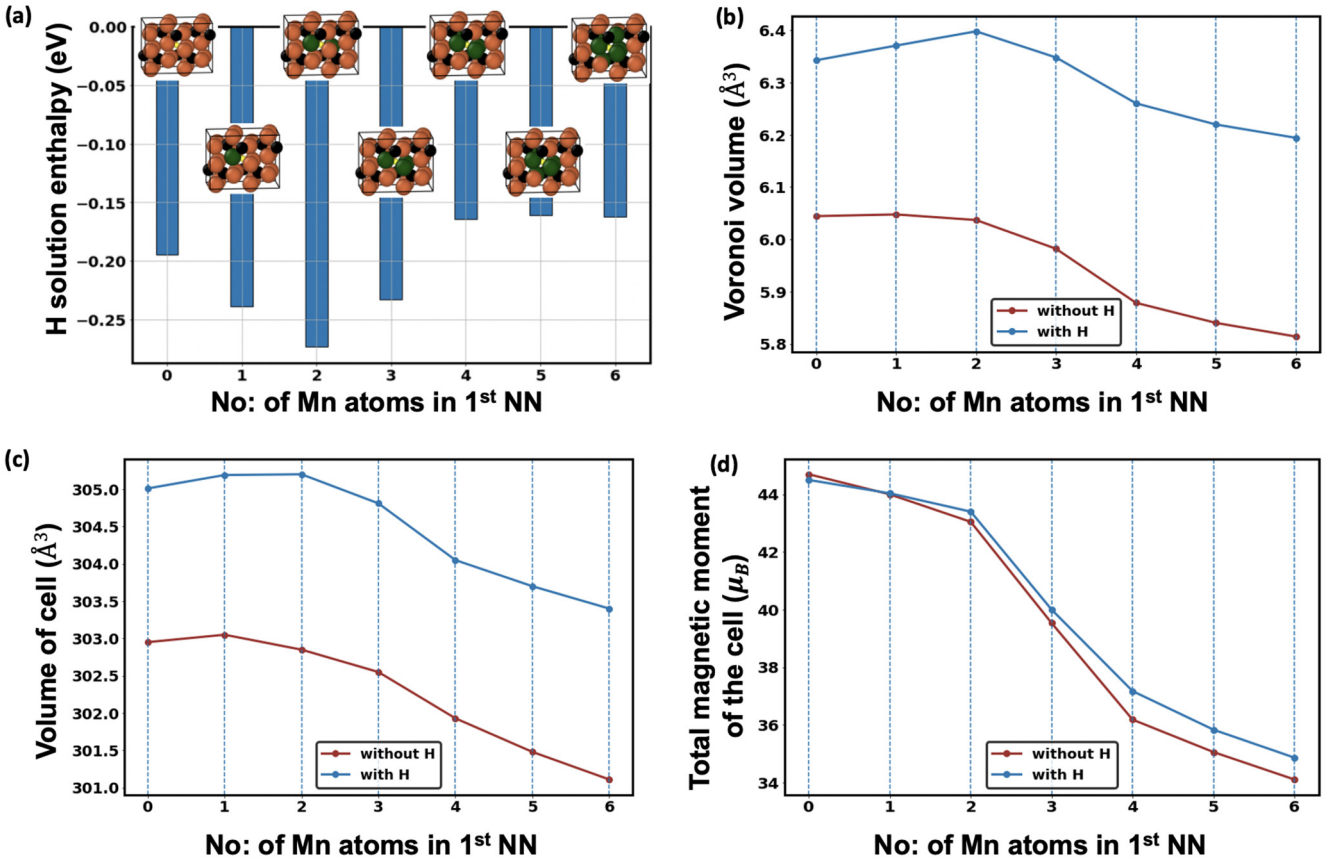

FIG. 4. (a) Solution enthalpies of a H atom in $(Fe,Mn)_3C$ with up to 6 Mn subsitutions that are limited to nearest neighbor sites of H. Variation of (b) Voronoi volume, (c) volume, and (d) total magnetic moment of the cell with and without H with respect to the number of nearest neighbor Mn atoms in the first shell around H in $(Fe,Mn)_3C$.

However, it turns out that the fundamental origin of these two different trends is largely the same. To this end, the Voronoi volume, an important descriptor for H in fcc Fe-Mn alloys, has been analyzed for the carbides. We observe that the solution enthalpy of H correlates with the variation in the Voronoi volume available for a H atom occupying an interstitial site [Fig. 4(b)].

More specifically, there is an overall decrease of the interstitial Voronoi volume with Mn additions due to the presence of C, which is opposite to the situation in the fcc bulk. Only the H atom situated in between the first two substituted Mn atoms is found to be increasing the interstitial site Voronoi volume [Fig. 4(b)], indicating the role of H in the relaxation of the carbides.

At the same time, substituted Mn atoms follow a concentration-dependent magnetic arrangement, as already observed for bcc Fe-Mn alloys [57]. The first two Mn atoms are aligned ferromagnetically with smaller moments with respect to the other Fe atoms, decreasing the total magnetic moment [Fig. 4(d)]. The next two Mn atoms align antiferromagnetically to the other Fe atoms, yielding a much steeper decrease of the total magnetic moment. These magnetic arrangements cause relaxation effects that yield a decrease in the Voronoi volume of the interstitial site.

Decoupling the solution enthalpies into a chemical and an elastic contribution [32] provides insights into the changes in solubility with these parameters. Here, the chemical contribution determines the chemical binding energy of H in a relaxed supercell of $(Fe,Mn)_3C$ and the elastic contribution results from the relaxation effect of H in this cell. Upon decoupling, it is found that the chemical contribution of the interstitial-H solution enthalpy is directly proportional to the Voronoi volume of H [Fig. 5(b)]. Hence the Mn atoms substituted locally around H control the Voronoi volume by a magnetovolume effect and therewith modify the chemical binding energy of the interstitial-H by the nearest-neighbor metal atoms. The reduced Voronoi volume of H goes along with a decrease in total volume of the cell [Figs. 4(b) and 4(c)], as it is evident from the expected proportionality between both volumes [Fig. 5(a)].

B. Study on the long-range influence of Mn on the H solubility in Fe_3C and $Fe_{23}C_6$

In order to understand the long-range influence of Mn atoms, we looked into the H solubility in Fe_3C and $Fe_{23}C_6$ with respect to Mn concentration following the strategy in Fig. 2(c). The variation in the H solubility for interstitial sites in $(Fe,Mn)_3C$ as well as C vacancy sites in $(Fe,Mn)_3C$ and $(Fe,Mn)_{23}C_6$ is shown in Fig. 6.

The H solution enthalpy has been found to be positive in all relevant interstitial sites of $(Fe,Mn)_{23}C_6$ and is, hence, not considered for the present study. The choice of interstitial lattice sites in $(Fe,Mn)_{23}C_6$ is taken from Ref. [58]. The solution

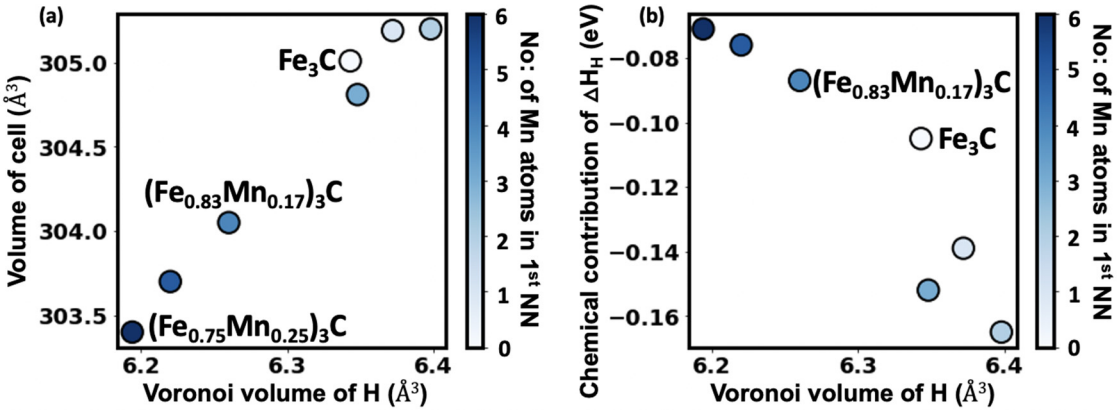

FIG. 5. Correlation between (a) the volume of the cell with H and (b) the chemical contribution of H solution enthalpy at the interstitial site of $(Fe,Mn)_3C$ as a function of Voronoi volume of the interstitial site with H.

enthalpies are subject to the choice of the H chemical potential reference. For the present study, the energy of an interstitial H atom in bcc Fe is considered as reference. Therefore, positive solution enthalpies indicate that H is preferred to stay in bcc Fe.

The differences in the observed trends are remarkable.

(i) The blue bars in Fig. 6 correspond to the solution enthalpy change with respect to Mn addition from ferromagnetic Fe_3C to ferrimagnetic Mn_3C for the interstitial-H. The solubility of H decreases till the concentration of Mn reaches approximately 2/3 in the metal sublattice and later increases with respect to Mn concentration following a concave curve (opposite to the trend in Fig. 4).

(ii) There exists an almost linear trend for the solubility of H in C vacancy sites of $(Fe,Mn)_3C$ (red bars), which is completely different from the interstitial case.

(iii) The solubility of H is significantly higher in the C vacancy of $(Fe,Mn)_{23}C_6$ (green bars) compared to the other carbide, especially for Mn concentrations of approximately 22%. The distinctive behavior of C vacancy-H follows a convex curve for the solubility in $(Fe,Mn)_{23}C_6$.

These differences in H solubility trends between short- vs long-range, interstitial vs vacancy, and Fe_3C vs $Fe_{23}C_6$ carbide type make it challenging to identify universal parameters describing the impact of Mn atoms on H incorporation in carbides. For the purpose of decoding the observed trends, we benefit from the short-range study in the previous section and look into the role of the Voronoi volume of H, the volume of the supercell, and the total magnetic moment of the supercell. Such an analysis for $(Fe,Mn)_3C$ is given in Fig. 7.

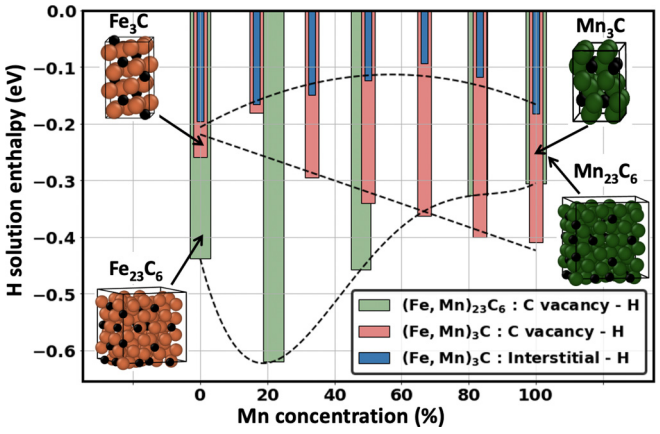

FIG. 6. Calculated solution enthalpies of H at interstitial and C vacancy positions in $(Fe,Mn)_3C$ and $(Fe,Mn)_{23}C_6$ with increasing concentration of Mn. The curves demonstrating the trends in solution enthalpies are plotted in black dash lines.

1. H solubility in interstitials in $(Fe,Mn)_3C$

In the case of interstitial-H, the important role of the Voronoi volume is confirmed in Fig. 7(b). After the first NN shell is fully filled, it decreases further, qualitatively consistent with the concave shape of the solution enthalpy, where the solubility minimum is observed at 67% (after the third NN shell is fully filled with Mn).

The long-range impact of Mn on the local Voronoi volume is again resulting from an interplay between volume and magnetism. Therefore, they need to be evaluated separately.

(i) Constrained volume calculations are employed by fixing the cell shape and volume for all compositions to that of Fe_3C (which is a larger volume than that of Mn_3C), but allowing internal relaxations of the atomic positions. Providing such a larger volume increases the local Voronoi volume [Fig. 7(b)] as well as the solubility [orange bars in Fig. 7(a)], once the second NN shell is filled with Mn.

(ii) The very low solubility of H observed in the nonmagnetic Mn-free Fe_3C compared to the magnetic Fe_3C [blue and gray bars in Fig. 7(a)] could again be linked to magnetovolume effects. The magnetic state of Fe implies a larger Voronoi volume for interstitial sites in magnetic Fe_3C [Fig. 7(b)], and hence the larger solubility of H. The solubility curve of nonmagnetic $(Fe,Mn)_3C$ is clearly correlated with the Voronoi volume, but also with the volume of the cell. In particular, after the filling of the first NN shell by H, there is a consistent increase of both volumes with the Mn content and hence an increase in solubility. This needs to be compared with the magnetic state, where an overall decrease of the cell volume with the Mn concentration is observed.

Remarkable are the Mn concentrations above 50%. Here, the magnetic and nonmagnetic volumetric slope is similar; the magnetic calculation yields the systematically larger volume, but the H solubility is higher for the nonmagnetic case. This

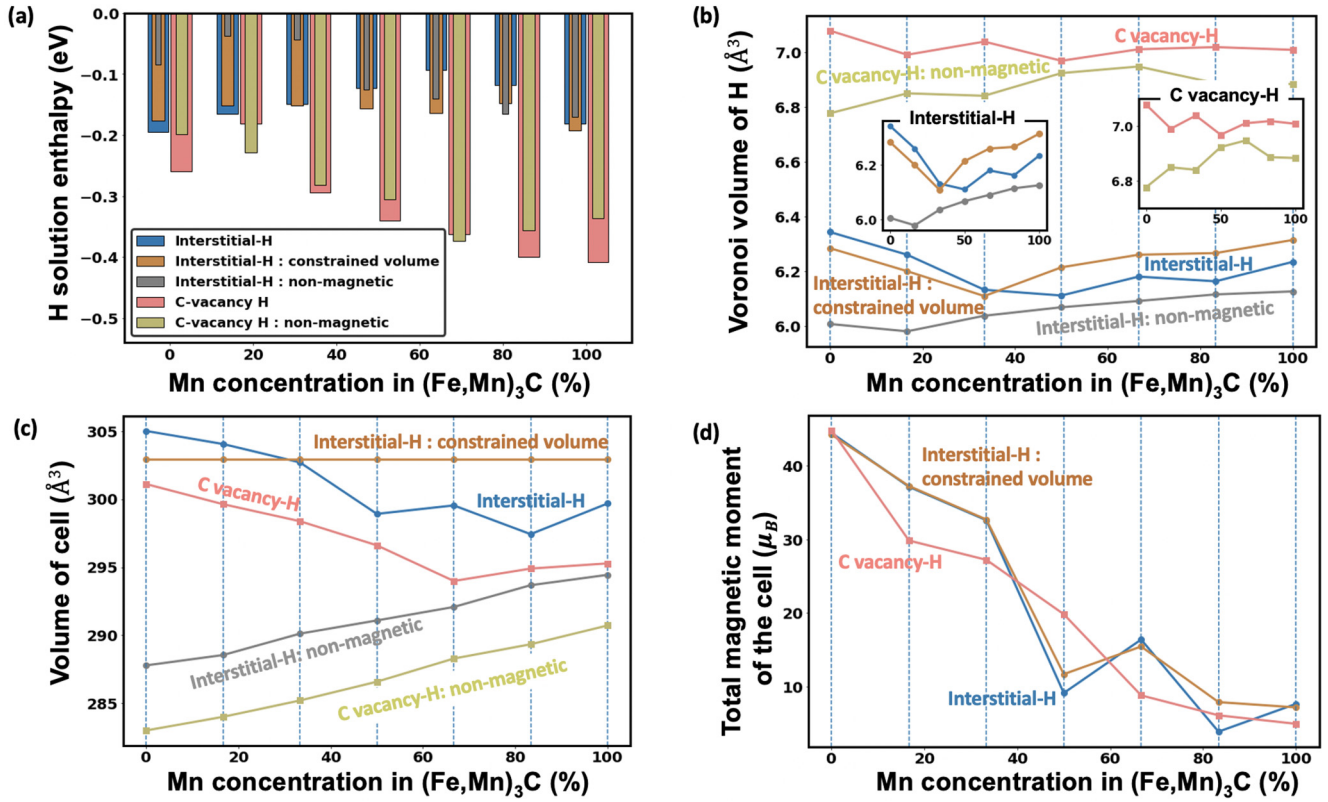

FIG. 7. (a) H solution enthalpies at the interstitials and C vacancy sites of $(Fe,Mn)_3C$ with respect to the Mn concentration. Blue bars correspond to the volume relaxed $(Fe,Mn)_3C$, whereas orange bars represent calculations where the volume is constrained to that of Fe_3C. Gray bars correspond to a set of nonmagnetic fully relaxed calculations. The H solubilities at C-vacancy sites with and without magnetism are denoted by the coral pink and olive-green bars, respectively. The variation of (b) the Voronoi volume, (c) the volume of the supercell, and (d) the total magnetic moment of the calculated supercell with respect to the increasing concentration of Mn are additionally provided.

indicates the detrimental effect of the ferrimagnetic order on the H chemical binding to the metal atoms, even if the total magnetic moment is close to zero [Fig. 7(d)]. Hence, in contrast to the occupation of the first NN shell with Mn atoms, which is related to a magneto-Voronoi volume coupling effect (Fig. 4), both magnetism and volumetric relaxations determine the long-range impact of Mn on H. The details discussed above will be reused for the correlative analysis described in the upcoming Sec. III E 1.

2. *H solubility in C vacancies in $(Fe,Mn)_3C$*

We next try to transfer the results obtained for the H solubility in an interstitial site to the H solubility inside a C vacancy. The latter shows a nearly linear trend with respect to Mn content for long-range interactions, while the Mn impact due to the filling of the first NN shell is different. The C vacant sites are better traps than interstitials in $(Fe,Mn)_3C$ due to the substantially larger Voronoi volume available for H in C vacancies compared to interstitial sites [Fig. 7(b)]. However, this larger Voronoi volume remains nearly the same throughout the concentration of Mn. Thus the Voronoi analysis explains why C vacancies are stronger H traps, but does not explain the change in solubility with respect to Mn concentration.

Again the change of the volume of the cell and the impact of magnetism seem to be important for the long-range impact of Mn. Remarkable in this case is that a decreasing cell volume yields an increase in the H solubility. Since the volume trend is opposite for the nonmagnetic case, the explicit dependence on magnetism seems to compensate the increasing volume trend such that the H solubility for the Mn occupation of the intermediate shells is almost the same for the magnetic and nonmagnetic case. The situation seems to be different for the Mn filling of the last shell, where the magnetic state has no impact on the trend for the cell volume, but determines the trend for the H solubility.

3. *H solubility in C vacancies in $(Fe,Mn)_{23}C_6$*

In the case of C vacancy-H in $(Fe,Mn)_{23}C_6$, the solubility is found to be increasing initially till ∼22% and then it decreases with further addition of Mn into the metal sublattice unlike the straightforward, nearly linear trend observed in the case of $(Fe,Mn)_3C$ (Fig. 6). Such a trend is not reflected directly in any of the features studied for most of the compositions (Fig. 8). In particular, the case of C vacancy in $(Fe,Mn)_{23}C_6$ does not show the same correlation to the Voronoi volume as in the case of $(Fe,Mn)_3C$ without vacancies. Instead, the magnetic state of $(Fe,Mn)_{23}C_6$ is found to be even more significant for the H solubility after performing an analysis in nonmagnetic $(Fe,Mn)_{23}C_6$ [Fig. 8(a)]. The addition of Mn to nonmagnetic $(Fe,Mn)_{23}C_6$ does not have any effect on the solubility of H at C vacancy sites. It is also found that the solubility of H in C vacancy sites of $Fe_{23}C_6$ is

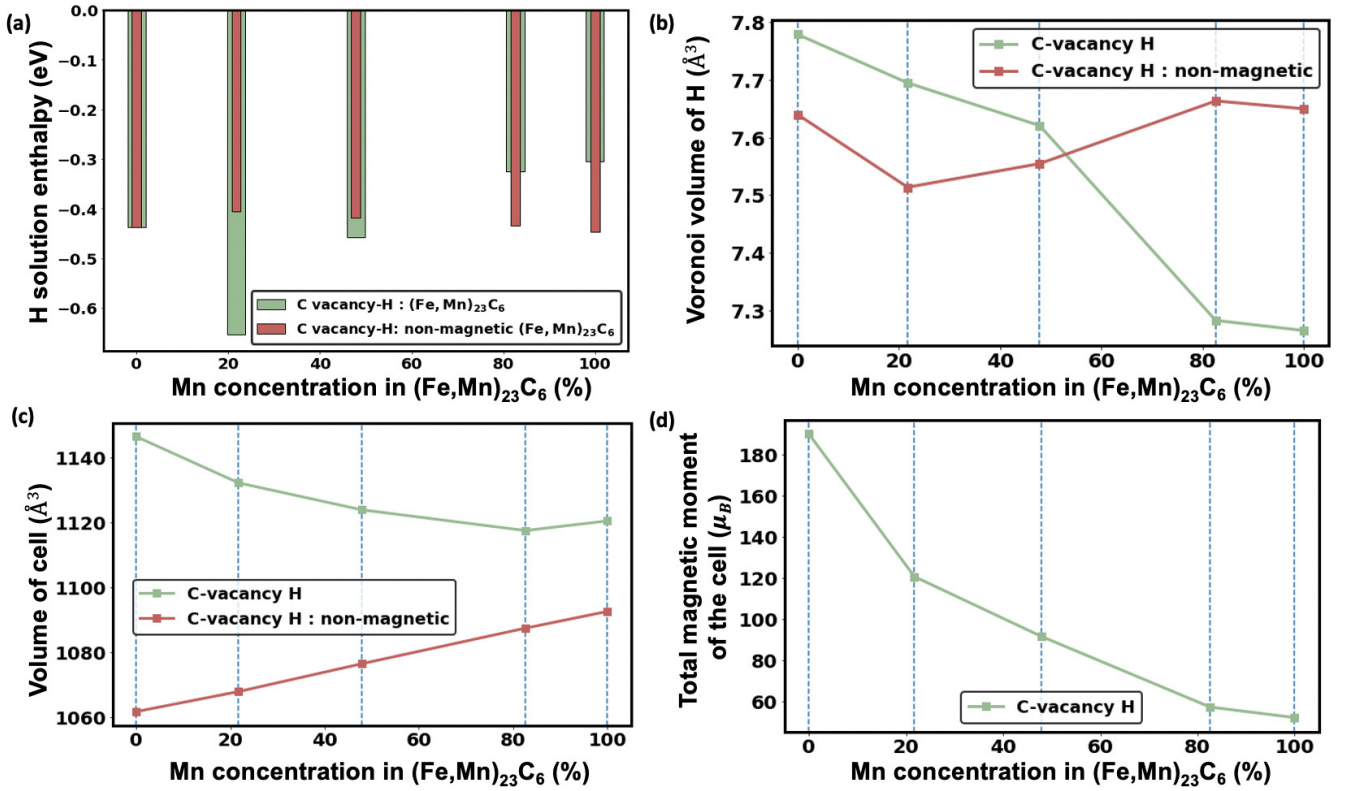

FIG. 8. (a) Calculated solution enthalpies of H at the C vacancy positions in Mn-containing $Fe_{23}C_6$ evaluated both magnetically and nonmagnetically with increasing concentration of Mn. Corresponding changes in (b) the Voronoi volume, (c) the volume of the cell, and (d) the magnetic moment of the cell are examined.

unaffected by switching off magnetism, irrespective of the change in Voronoi volume of H. However, the magnetic state of the Mn atoms is crucial for the C vacancy-H solubility in $Mn_{23}C_6$.

Therefore, H in the presence of Mn behaves differently in different carbides, in different sites, and at different ranges. It is a demanding procedure to unravel a small set of descriptors to describe all these different trends. A common feature seems to be, however, that the trends on Mn concentration depend on the NN shell being filled. In Sec. III E, we will therefore use this observation for dealing with the complex behavior in solubilities due to the presence of Mn-like elements.

C. Study on the short-range influence of Cr on H solubility in Fe_3C

Similar to Mn, we also investigate the change in solution enthalpy of H in an octahedral interstitial site of cementite as a function of Cr atoms in the neighboring shells of H. There exists a nearly linear trend in the solubility with respect to the increase in number of Cr atoms in the first NN shell around H. For the first few Cr atoms, the local Voronoi volume changes similarly to the Mn case, but it levels off when the first NN shell is filled [Fig. 9(b)]. Moreover, the trend of the global volume of the cell is different [Fig. 9(c)]. Therefore, the volumetric impact on the H solubility seems to be less relevant in the case of Cr substitution.

Instead, there is a reduction in the total magnetic moment of the system, which is nearly consistent with the reduction in solution enthalpy [Figs. 9(a) and 9(d)]. Cr does not show a pronounced concentration-dependent magnetic arrangement as in the case of Mn (cf. Sec. III A), but Cr atoms are aligned antiferromagnetically to the other Fe atoms. This magnetic moment reduction appears to be controlling the solubility profile of a H atom in the interstitial site.

D. Study on the long-range influence of Cr on H solubility in Fe_3C and $Fe_{23}C_6$

In Fig. 10, the solubilities of H in the interstitial sites and C vacant sites are plotted as a function of the long-range Cr content in the metal sublattice of Fe_3C and $Fe_{23}C_6$, again using the strategy illustrated in Fig. 2. As H has a positive solution enthalpy at the interstitial sites in $(Fe,Cr)_{23}C_6$ for the chosen chemical potential reference of H, these sites are not included in Fig. 10.

The most obvious conclusion from Fig. 10 is the high solubility of H in C vacancy sites as compared to that in interstitial sites, irrespective of the type of carbide and Cr content in them. This behavior of C vacancy sites is associated with their larger Voronoi volume available for H as compared to the interstitials (Fig. 11). As discussed in Sec. III B, this is true for Mn substituted Fe_3C and $Fe_{23}C_6$ as well.

The H atoms in C vacancies behave similarly in both Cr containing Fe_3C and $Fe_{23}C_6$. The solubility increases with

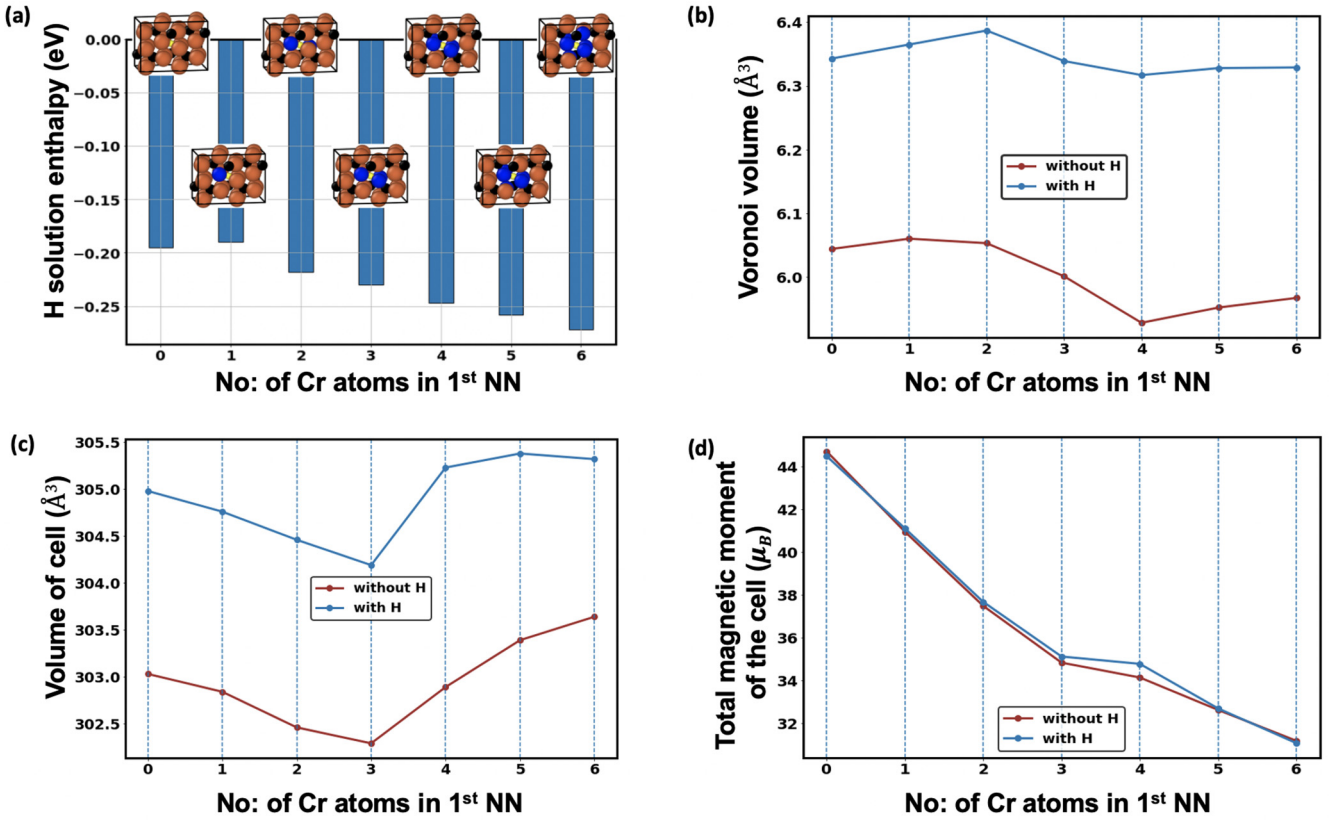

FIG. 9. (a) Solution enthalpy of H at the interstitial site of $(Fe,Cr)_3C$ up to 6 Cr nearest neighbors of H. Variation of (b) the Voronoi volume, (c) the volume of the supercell used for calculation, and (d) the total magnetic moment of the calculated supercell with respect to the number of NN Cr atoms in the first shell around H in $(Fe,Cr)_3C$.

increase in Cr content up to a concentration of approximately 25%, beyond which the values remain almost constant. An analogous trend is visible for interstitial-H with increasing Cr concentration, though the fitted line is linear. The increase in solubility in the latter case is visible even beyond the filling of the first and second NN shell and persists until the third NN shell (the first 14 metal atoms around H) is filled with Cr.

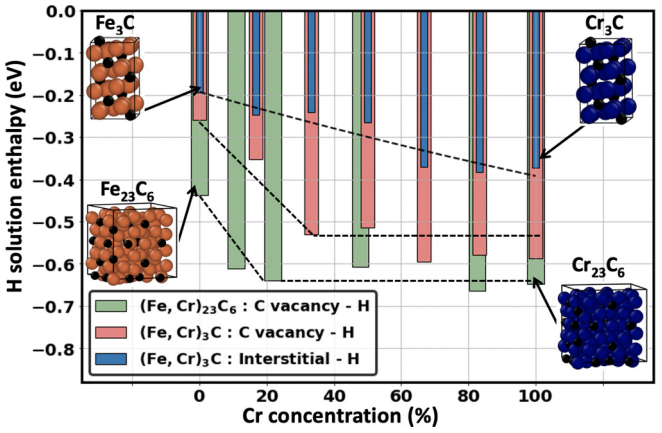

FIG. 10. Calculated solution enthalpies of H at interstitial and C vacancy positions in Cr-containing $Fe_{23}C_6$ and cementite with increasing concentration of Cr. The interstitial-H solubility of $(Fe,Cr)_{23}C_6$ are highly unfavorable and therefore not plotted here. The trend in solubilities are marked in black dashed line.

1. H solubility in interstitials in $(Fe,Cr)_3C$

To determine the reason behind the observed trends of H solubility in interstitials in $(Fe,Cr)_3C$, we investigate in Fig. 11 the same dependencies for Cr as in Fig. 7 for Mn. Though the Voronoi volume is not considered as a main parameter for explaining the solubility trend in the short-range (first NN) interactions [Figs. 9(a) and 9(b)], it appears to strongly correlate with the observed global trend in solubility of interstitial-H [Figs. 11(a) and 11(b)].

The total volume of the cell remains constant up to 50% of Cr content in the metal sublattice of $(Fe,Cr)_3C$ and then it increases with further Cr content. By constraining the volume of the cell for all configurations to the volume of Fe_3C (smaller volume than that of Cr_3C), we found that the solubility trend remains unchanged, making the volume of the cell a less significant parameter. The values of solubility are slightly lower than the unconstrained solubility values for higher Cr content, which is explainable from the lower Voronoi volume of H due to the reduced cell volume.

A common phenomenon, occurring very similarly in constrained and unconstrained volume cases, is the transition of the magnetic state of Fe_3C with Cr addition. It produces a similar variation in the Voronoi volume and the solubility of H. At the same time, nonmagnetic calculations confirm the importance of magnetism for the short-range impact of Cr on the solubility of H in the interstitial site [Fig. 11(a)]. The H solubility in nonmagnetic $(Fe,Cr)_3C$ is very similar to that

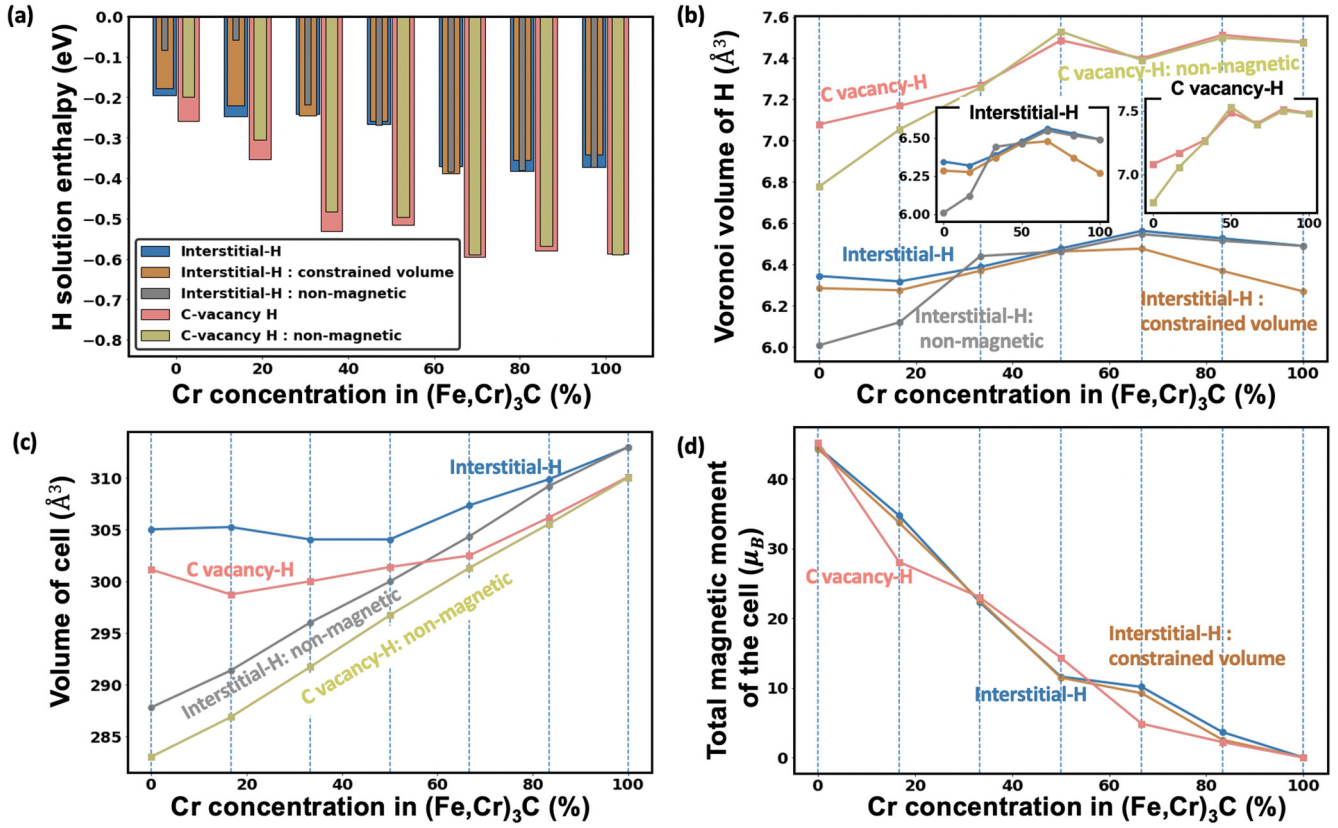

FIG. 11. (a) H solution enthalpies at both the interstitials and C vacancy sites of $(Fe,Cr)_3C$ with respect to the Cr concentration in the Fe sublattice of cementite. The meaning of the bars is identical to Fig. 7. Further, the variation of (b) the Voronoi volume, (c) the volume of the supercell, and (d) the total magnetic moment of the supercell with the concentration of Cr is displayed.

of magnetic $(Fe,Cr)_3C$ for the filling of the other shells with Cr, which is also evident from the corresponding Voronoi volumes. The short-range and long-range influence of Cr in Fe-C environment discussed above will be used for describing correlations in Sec. III E 1.

2. *H solubility in C vacancies in $(Fe,Cr)_3C$*

Similar to the Mn case, C vacancies in $(Fe,Cr)_3C$ are found to be better traps for H over interstitial sites and this is consistent with the increased Voronoi volume of H in the case of C vacancies. Further, there is an increase in solubility with increase in Cr content till the second NN shell (eight metal atoms) is fully filled with Cr, and it remains constant when the Cr content is further increased [Fig. 11(a)]. The same pattern is observed for the Voronoi volume of H over Cr content [Fig. 11(b)], making it again one major parameter controlling the solubility of H in C vacancies. Finally, the similarity of this solubility in $(Fe,Cr)_{23}C_6$ and in $(Fe,Cr)_3C$ (Fig. 10) supports the assumption that the impact of the Cr content on the solubility of H in C vacancies follows for all carbides the same trend.

E. *Ab initio* informed predictions of H solubility in M_3C carbides

Based on the above presented in-depth studies on decoding chemical trends, several conclusions on the role of Cr and Mn on solubility profiles of interstitial-H and C vacancy-H are derived. (i) In the case of Mn, the Voronoi volume and strong magnetovolume effects explain the short-range impact of alloying, but this seems to be less relevant for Cr. (ii) The long-range impact of alloying on the solubility of interstitial-H is dominated by the Voronoi volume in the case of Cr, but is more sophisticated in the case of Mn. (iii) The H solubility in the C vacancy of $(Fe,Mn)_{23}C_6$ is associated with the magnetic state of atoms, whereas the same of $(Fe,Mn)_3C$ is difficult to understand. (iv) The influence of Cr on the solubility of H in a C vacancy site of $(Fe,Cr)_3C$ and $(Fe,Cr)_{23}C_6$ and the interstitial site of $(Fe,Cr)_3C$ can only be correlated to the cell volume and the magnetism for the first few NN shells.

Despite this apparent diversity in the physical understanding, the different trends in common have a significant correlation between the concentration of alloying elements and the H solubility. The observed correlations show a qualitatively different character for the first and the other NN shells with respect to the H position. In general, the occupation of NN shells appears to be a good descriptor to predict the nonmonotonic slope changes in the solubility trends.

1. *Correlation analysis: Binary-metal M_3C carbides*

In the following sections, the representation of a carbide as $(A,B)_3C$ indicates that B is alloyed in the metal sublattice of A with respect to nearest-neighbor distances [using the approach in Figs. 2(b) and 2(c)]. Using the data from the H solubility studies in $(Fe,Cr)_3C$ and $(Fe,Mn)_3C$, one can derive the behavior of Cr and Mn around H in Fe-C environments.

We try to expand these conclusions to other binary-metal carbides of Fe, Cr, and Mn.

The studies on the impact of Mn on the H solubility yield a decreasing trend until the third NN shell around H is fully filled with Mn and then an increase with further addition of Mn till Mn_3C. This trend is explained by a direct connection between solubility and Voronoi volume in the first and second NN shell, and the importance of coupled volumetric and magnetic relaxations in cementite after the second NN shell. Now if one studies the impact of Mn on H solubility in $(Cr,Mn)_3C$, according to the behavior of Mn in H containing $(Fe,Mn)_3C$, we would expect a nearly similar concave shaped curve of H solution enthalpy.

Similarly, one aspect about Cr around interstitial-H in Fe_3C is that the solubility of H increases with increase in Cr concentration. This variation in solubility, as mentioned earlier, can be explained in terms of the changes in the Voronoi volume and volume of the cell along with the magnetic to nonmagnetic transition of the system with the addition of more Cr into cementite. Using these insights, one expects a similar trend for the impact of Cr on H solubility in $(Mn,Cr)_3C$ as in $(Fe,Cr)_3C$, i.e., an increase in solubility with increasing Cr concentration. We note that the paths $(Mn,Cr)_3C$ and $(Cr,Mn)_3C$ are not mirrored, because the first Cr atoms in the former case occupy [using the approach in Figs. 2(b) and 2(c)] the first NN shell of H, while the last Cr atoms in the latter case occupy shells further away from the H atom.

In order to assess the quality of these predictions, we studied the variation in H solubility from Cr_3C to Mn_3C, considering all the intermediate concentrations of Mn, and compared it with $(Fe,Mn)_3C$ as shown in Fig. 12(a). Along with this, we compared $(Fe,Cr)_3C$ with $(Mn,Cr)_3C$, where H has Cr nearest neighbors in the beginning [Fig. 12(b)]. As expected, the Mn occupation of sites closer to H yields a decrease in the solubility of H. Also Cr atoms as nearest neighbors of H decrease the solution enthalpy of H [Fig. 12(b)]. These figures confirm a strong correlation of the Mn trends in $(Fe,Mn)_3C$ and $(Cr,Mn)_3C$ and show an even better correlation of the Cr trends in $(Fe,Cr)_3C$ and $(Mn,Cr)_3C$. This opens the possibility to predict H solution enthalpies of mixed alloys of carbides containing Cr, Mn, and Fe. Due to the complex magnetic and chemical interactions that exist in mixed metal carbides, the calculation of the solution enthalpy profile of H in them is computationally expensive when using first principles DFT. Machine learning approaches could prove to be helpful in dealing with such complex alloys. Hence, in the next section, we provide the results of a simple machine learning approach.

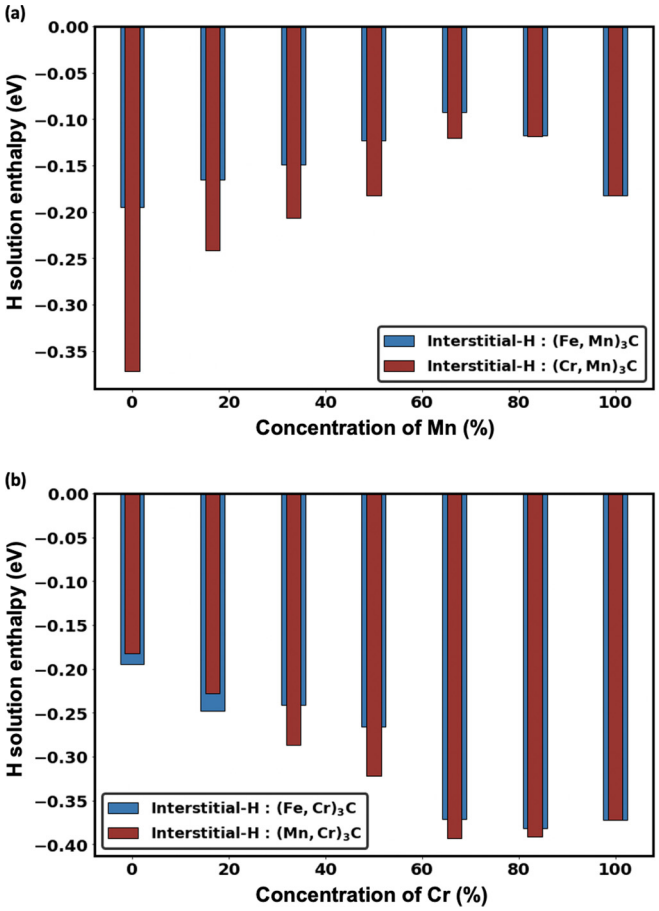

FIG. 12. Calculated solution enthalpies of H at an interstitial position in (a) Mn-containing Fe_3C and Cr_3C with increasing concentration of Mn and (b) Cr-containing Fe_3C and Mn_3C with increasing concentration of Cr.

2. *Machine learning*

Using the limited DFT data (due to the complicated interplay of magnetism and chemistry) that we generated for the binary-metal carbides as a training set, we design a machine learning model based on ridge regression where the nearest-neighbor atom types around H serve as the input feature list. For designing the model, we divide the supercell with H into four nearest-neighbor shells and provided the model with the information of the number of Cr, Mn, and Fe atoms in each shell. In this way, the training set contains the values of the H solution enthalpy in binary-metal carbides, associates it with the number of Fe, Cr, and Mn atoms in the shells, and the model predicts the H solution enthalpy values for ternary-metal carbides. The information of physical attributes is therefore implicitly considered. This is because the effect of the physical attributes on the solubility of H in each composition of a carbide is itself dependent on the number of corresponding metal atoms for a given composition and its distribution according to the NN principles.

The model successfully predicts the solution enthalpy of H in ternary-metal carbides with a mean absolute percentage error around 10%. Figure 13 shows the correlation between calculated and predicted solution enthalpies of H in (Fe-Cr-Mn) ternary- and different (Fe-Cr), (Fe-Mn), and (Cr-Mn) binary-metal mixture carbides. Random spatial arrangements of Cr and Mn are chosen for constructing the configurations for the ternary-metal carbides. This indicates the quality of the fit and is therefore a measure of how well solubilities in such carbides are predicted by the model.

Since the validation of the model for the quinary $(Fe,Cr,Mn)_3C$-H systems yields acceptable errors, we apply it to predict the solubility behavior of H for compositions for which extensive DFT calculations are not feasible. To relate with the real world scenarios, the chemical potential

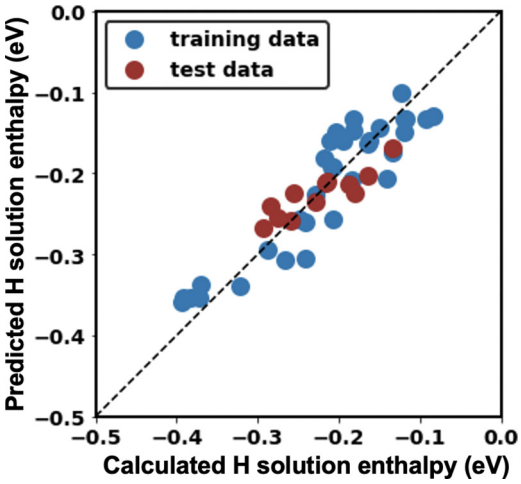

FIG. 13. Predicted solution enthalpies of H at interstitial positions in binary-metal carbides (DFT training set) and ternary-metal carbides (DFT test set) plotted against the calculated solution enthalpies of the same.

reference of H is chosen from rain water for the ternary-metal carbides ($\mu^{H}_{\text{rainwater}} = -0.33$ eV with respect to H_2 molecule, taken from Ref. [59], p. 8). The solubility of H is expressed in terms of H concentration in these multicomponent carbides using the Boltzmann relation [Eq. (4)], and the corresponding concentration values are represented in the form of heat maps as shown in Fig. 14.

The heat maps of H concentration indicate that only a small composition range gives rise to a strong increase in H solublity in $(Fe,Cr,Mn)_3C$, represented by the red zone in the figure. More specifically, these are carbides that are rich in Cr and contain an intermediate amount (12–30%) of Mn. Interestingly, a small amount of Fe in Cr-rich cementite has a similar impact as Mn, while Mn and Fe together have a smaller impact. While qualitatively the distributions remain at higher temperatures (Fig. 14, 650 K), a much broader range of Cr rich $(Fe,Cr,Mn)_3C$ carbides then contains a substantial amount of H, indicated by the shading in the upper corner of the triangular heat map. Even peak concentrations above 10 at. % H can be reached. Figure 14 can, therefore, provide a picture about the H-carbide interactions in multicomponent carbides, which are often observed in steels. In this regard, the heat maps from machine learning predictions can serve as a guide to the R & D engineers, especially to tailor microstructural components via alloying for improving other mechanical properties.

The accuracy of the model can be improved with an availability of finer mesh of data on binary-metal carbides. In future, the quality of the model could be improved to identify attributes (like Voronoi volume) that are responsible for the H solubility in ternary- and quaternary-metal carbides.

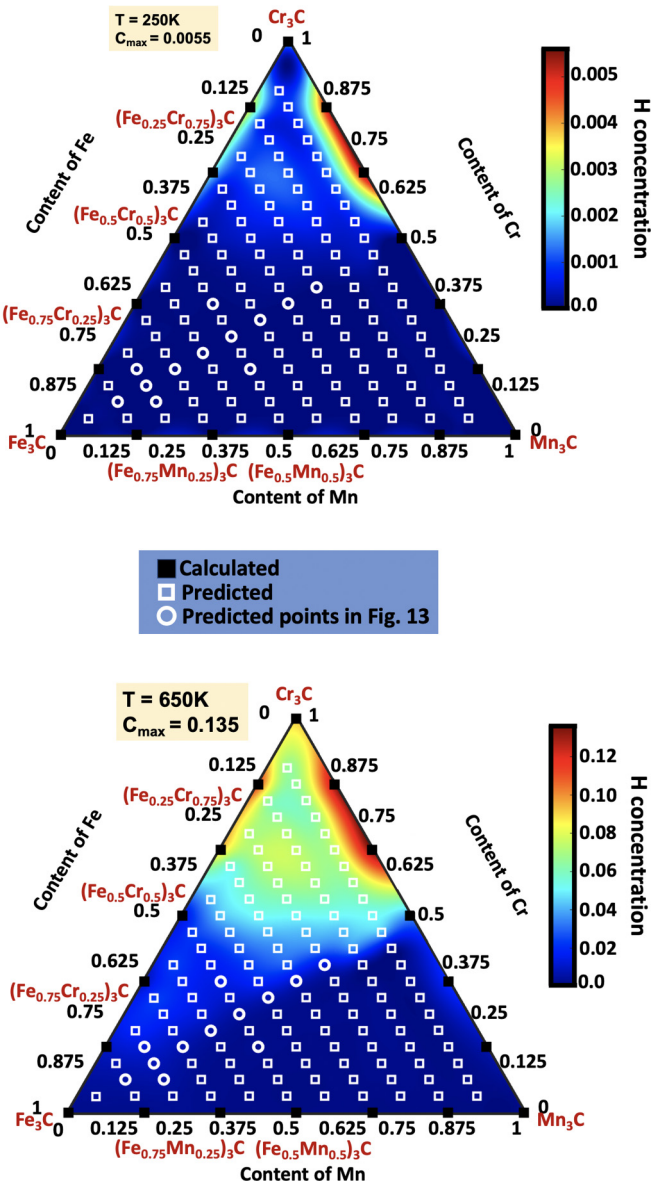

FIG. 14. Heat maps of H concentration in $(Fe,Cr,Mn)_3C$ carbides at two different temperatures is plotted in the form of a Gibbs triangle. The black-filled squares along the border of the triangle correspond to the H concentration values obtained using *ab initio* calculations in binary-metal carbides and the white nonfilled squares inside the triangle represent the H concentration values in ternary-metal carbides from the machine learning model. The white nonfilled circles in the triangle correspond to the test set of the model. The projected heat maps of the H concentration are obtained by employing a cubic interpolation scheme on the data points.

IV. CONCLUSION

The role of alloying in carbides, especially by Cr and Mn, on H solubility is prototypically investigated for Fe_3C and $Fe_{23}C_6$. To this end, the analysis addresses two major challenges: (i) an in-depth study that focuses on identifying the physical descriptors responsible for the nonmonotonic H solubility trends in ternary Fe-Mn-C and Fe-Cr-C systems and (ii) the implementation of an *ab initio* informed ridge regression model for predicting the H solubility in complex ternary-metal carbides (Fe-Mn-Cr-C) using the DFT data of different binary-metal carbides.

In the case of Cr alloying, the H solubility trends in the carbides with respect to system, site, and range are similar. The interstitial-H solubility shows in general a linear trend

with Cr concentration in both the long range and the short range. This is mainly because of the magnetic transition that occurs in the $(Fe,Cr)_3C$ system (that is, a transition from ferromagnetic Fe_3C to nonmagnetic Cr_3C). Also, the solubility of H at C vacancy sites of $(Fe,Cr)_3C$ and $(Fe,Cr)_{23}C_6$ shows analogous trends.

In contrast to Cr, Mn alloying yields different, complex solubility trends for H at different trapping sites in the studied carbides. Due to such nonanalogous H-solubility trends, we can understand that the H-Mn interactions are system dependent, site dependent, and range dependent. Though there exists little similarity in H-solubility trends, the physical descriptors responsible for observed trends are largely the same. The solubility is dominated by the local atomic structure, as described by the Voronoi volume. However, the latter heavily depends on the coupling to the short- and long-range magnetic interactions and the resulting global volume of the supercell. The magnetovolume coupling of Fe-Mn carbides, therefore, explains the observed nonmonotonic solubility trends.

The transferability of the observations from $(Fe,Mn)_3C$ and $(Fe,Cr)_3C$ to other binary-metal carbides such as $(Cr,Mn)_3C$ and $(Mn,Cr)_3C$ are tested. It has been found that the role of Mn and Cr on H solubility is qualitatively the same in $(Fe,Mn)_3C$ and $(Cr,Mn)_3C$, and $(Fe,Cr)_3C$ and $(Mn,Cr)_3C$ at short and long range. This can be interpreted in terms of the arrangement of chemical species in nearest-neighbor shells around H. Based on these insights, the H solution enthalpies in $(Fe,Cr,Mn)_3C$ systems is described by machine learning using a ridge regression model. The model allowed us to successfully predict the H solubility in complex ternary-metal carbides that are difficult to model. The developed methodology can be extended to explore H solubility in other microstructural features such as complex carbide-matrix interfaces.

ACKNOWLEDGMENTS

The authors acknowledge the support from Z. Georgeou and F. Klose (Salzgitter Mannesmann Forschung GmbH, Salzgitter, Germany) for preparing the industrial samples and fruitful discussions. M. Nellessen (Department of Microstructure Physics and Alloy Design, MPIE) is greatly acknowledged for her assistance in EDX and EBSD analyses.

[1] D. Barbier, N. Gey, S. Allain, N. Bozzolo, and M. Humbert, Mater. Sci. Eng., A **500**, 196 (2009).
[2] O. Grässel, L. Krüger, G. Frommeyer, and L. Meyer, Int. J. Plast. **16**, 1391 (2000).
[3] B. C. De Cooman, *Automotive Steels*, edited by R. Rana and S. B. Singh (Woodhead Publishing, 2017), pp. 317–385.
[4] C. Scott, S. Allain, M. Faral, and N. Guelton, Rev. Métallurg. **103**, 293 (2006).
[5] J. P. Hirth, Metall. Trans. A **11**, 861 (1980).
[6] M. Koyama, E. Akiyama, Y.-K. Lee, D. Raabe, and K. Tsuzaki, Int. J. Hydrogen Energy **42**, 12706 (2017).
[7] H. K. Birnbaum and P. Sofronis, Mater. Sci. Eng., A **176**, 191 (1994).
[8] Q. Liu, J. Venezuela, M. Zhang, Q. Zhou, and A. Atrens, Corros. Sci. **111**, 770 (2016).
[9] M. Nagumo, Mater. Sci. Technol. **20**, 940 (2004).
[10] G. Lovicu, M. Bottazzi, F. Dâaiuto, M. De Sanctis, A. Dimatteo, C. Santus, and R. Valentini, Metall. Mater. Trans. A **43**, 4075 (2012).
[11] S. L. I. Chan, J. Chin. Inst. Eng. **22**, 43 (1999).
[12] J. Lee, T. Lee, Y. J. Kwon, D.-J. Mun, J.-Y. Yoo, and C. S. Lee, Met. Mater. Int. **22**, 364 (2016).
[13] X. Cheng, X. Cheng, C. Jiang, X. Zhang, and Q. Wen, Mater. Lett. **213**, 118 (2018).
[14] T. A. Timmerscheidt, P. Dey, D. Bogdanovski, J. Von Appen, T. Hickel, J. Neugebauer, and R. Dronskowski, Metals **7**, 264 (2017).
[15] H. K. D. H. Bhadeshia, ISIJ Int. **56**, 24 (2016).
[16] D. Raabe, H. Springer, I. Gutiérrez-Urrutia, F. Roters, M. Bausch, J.-B. Seol, M. Koyama, P.-P. Choi, and K. Tsuzaki, JOM **66**, 1845 (2014).
[17] T. Ramjaun, S. Ooi, R. Morana, and H. Bhadeshia, Mater. Sci. Technol. **34**, 1737 (2018).
[18] N. Medvedeva, I. Shein, M. Konyaeva, and A. Ivanovskii, Phys. Met. Metallogr. **105**, 568 (2008).
[19] M. Konyaeva and N. Medvedeva, Phys. Solid State **51**, 2084 (2009).
[20] J. H. Jang, I. G. Kim, and H. Bhadeshia, *Materials Science Forum* (Trans Tech Publ, Chicago, IL, 2010), Vol. 638, pp. 3319–3324.
[21] H. Sun, B. Giron-Palomares, W. Qu, G. Chen, and H. Wang, J. Alloys Compd. **803**, 250 (2019).
[22] A. Grajcar, M. Kciuk, S. Topolska, and A. Płachcińska, J. Mater. Eng. Perform. **25**, 2245 (2016).
[23] C. M. Fang, M. H. F. Sluiter, M. A. van Huis, C. K. Ande, and H. W. Zandbergen, Phys. Rev. Lett. **105**, 055503 (2010).
[24] C. Fang, M. Van Huis, M. Sluiter, and H. Zandbergen, Acta Mater. **58**, 2968 (2010).
[25] A. Bowman, G. Arnold, E. Storms, and N. Nereson, Acta Crystallogr., Sect. B: Struct. Crystallogr. Cryst. Chem. **28**, 3102 (1972).
[26] J. Xie, J. Shen, N. Chen, and S. Seetharaman, Acta Mater. **54**, 4653 (2006).
[27] H. Kleykamp, J. Alloys Compd. **321**, 138 (2001).
[28] Y. Li, Y. Gao, B. Xiao, T. Min, Y. Yang, S. Ma, and D. Yi, J. Alloys Compd. **509**, 5242 (2011).
[29] K. O. Henriksson, N. Sandberg, and J. Wallenius, Appl. Phys. Lett. **93**, 191912 (2008).
[30] Y.-S. Chen, H. Lu, J. Liang, A. Rosenthal, H. Liu, G. Sneddon, I. McCarroll, Z. Zhao, W. Li, A. Guo *et al.*, Science **367**, 171 (2020).
[31] T. Hickel, R. Nazarov, E. McEniry, G. Leyson, B. Grabowski, and J. Neugebauer, JOM **66**, 1399 (2014).
[32] J. Von Appen, R. Dronskowski, A. Chakrabarty, T. Hickel, R. Spatschek, and J. Neugebauer, J. Comput. Chem. **35**, 2239 (2014).

[33] E. J. McEniry, T. Hickel, and J. Neugebauer, Acta Mater. **150**, 53 (2018).
[34] C. Fang, M. Van Huis, and M. Sluiter, Acta Mater. **103**, 273 (2016).
[35] B. G. Lyashchenko and L. M. Sorokin, Sov. Phys. Crystallogr. **8**, 300 (1963).
[36] A. Tauqir, H. Nowotny, and P. R. Strutt, Metall. Trans. A **21**, 3021 (1990).
[37] S. Kiranbabu, P.-Y. Tung, L. Sreekala, T. Prithiv, T. Hickel, R. Pippan, L. Morsdorf, and M. Herbig, Mater. Sci. Eng., A 142372 (2021).
[38] V. I. Voronin, I. Berger, Y. N. Gornostyrev, V. Urtsev, A. Kuznetsov, and A. Shmakov, JETP Lett. **91**, 143 (2010).
[39] P. Hohenberg and W. Kohn, Phys. Rev. **136**, B864 (1964).
[40] W. Kohn and L. J. Sham, Phys. Rev. **140**, A1133 (1965).
[41] G. Kresse and D. Joubert, Phys. Rev. B **59**, 1758 (1999).
[42] J. P. Perdew, K. Burke, and M. Ernzerhof, Phys. Rev. Lett. **77**, 3865 (1996).
[43] G. Kresse and J. Hafner, Phys. Rev. B **48**, 13115 (1993).
[44] G. Kresse, J. Non-Cryst. Solids **192-193**, 222 (1995).
[45] G. Kresse and J. Furthmüller, Phys. Rev. B **54**, 11169 (1996).
[46] G. Kresse and J. Furthmüller, Comput. Mater. Sci. **6**, 15 (1996).
[47] P. E. Blöchl, Phys. Rev. B **50**, 17953 (1994).
[48] H. J. Monkhorst and J. D. Pack, Phys. Rev. B **13**, 5188 (1976).
[49] M. Methfessel and A.T. Paxton, Phys. Rev. B **40**, 3616 (1989).
[50] A. Dick, F. Körmann, T. Hickel, and J. Neugebauer, Phys. Rev. B **84**, 125101 (2011).
[51] E. Duman, M. Acet, E. F. Wassermann, J. P. Itié, F. Baudelet, O. Mathon, and S. Pascarelli, Phys. Rev. Lett. **94**, 075502 (2005).
[52] R. Sahara, T. Matsunaga, H. Hongo, and M. Tabuchi, Metall. Mater. Trans. A **47**, 2487 (2016).
[53] A. F. Guillermet and G. Grimvall, J. Phys. Chem. Solids **53**, 105 (1992).
[54] A. Y. Ng, *Proceedings of the Twenty-First International Conference on Machine Learning* (Association for Computing Machinery, New York, NY, 2004), p. 78.
[55] K. Kawakami and T. Matsumiya, ISIJ Int. **53**, 709 (2013).
[56] L. Ismer, T. Hickel, and J. Neugebauer, Phys. Rev. B **81**, 094111 (2010).
[57] A. Schneider, C.-C. Fu, O. Waseda, C. Barreteau, and T. Hickel, Phys. Rev. B **103**, 024421 (2021).
[58] J.-L. Cao, W. Xiao, Q. Cao, and B.-L. He, Fusion Sci. Technol. **74**, 177 (2018).
[59] R. Nazarov, T. Hickel, and J. Neugebauer, Phys. Rev. B **82**, 224104 (2010).